University of Kent

Kent Academic Repository

Cernat, Ramona, Uceda, Adrian Fernandez, Marques, Manuel, Jimenez, Alejandro Martinez and Podoleanu, Adrian (2026) *Real-time en-face optical coherence tomography using a 9 GHz photodetected signal*. Optics Express, 34 (20). pp. 37906-37923. ISSN 1094-4087.

Downloaded from
https://kar.kent.ac.uk/116727/ The University of Kent's Academic Repository KAR

The version of record is available from
https://doi.org/10.1364/OE.603788

This document version
Publisher pdf

DOI for this version

Licence for this version
CC BY (Attribution)

Additional information

Versions of research works

Versions of Record
If this version is the version of record, it is the same as the published version available on the publisher's web site. Cite as the published version.

Author Accepted Manuscripts
If this document is identified as the Author Accepted Manuscript it is the version after peer review but before type setting, copy editing or publisher branding. Cite as Surname, Initial. (Year) 'Title of article'. To be published in ***Title of Journal*** , Volume and issue numbers [peer-reviewed accepted version]. Available at: DOI or URL (Accessed: date).

Enquiries
If you have questions about this document contact ResearchSupport@kent.ac.uk. Please include the URL of the record in KAR. If you believe that your, or a third party's rights have been compromised through this document please see our Take Down policy (available from https://www.kent.ac.uk/guides/kar-the-kent-academic-repository#policies).

Research Article | Vol. 34, No. 20 / 5 Oct 2026 / Optics Express 37906
Optics EXPRESS

Real-time *en-face* optical coherence tomography using a 9 GHz photodetected signal

RAMONA CERNAT,[1,*] ADRIAN FERNANDEZ UCEDA,[1] MANUEL MARQUES,[1] ALEJANDRO MARTINEZ JIMENEZ,[1,2,3] AND ADRIAN PODOLEANU[1]

[1]*Applied Optics Group, School of Engineering, Mathematics and Physics, University of Kent, Canterbury CT2 7NH, United Kingdom*
[2]*Departamento de Física, Universidad de Castilla-La Mancha, Campus de la Fábrica de Armas, 45071, Toledo, Spain*
[3]*Institute of Nanoscience, Nanotechnology and Molecular Materials (INAMOL), Universidad de Castilla-La Mancha, Campus de la Fábrica de Armas, 45071 Toledo, Spain*
[*]*R.Cernat@kent.ac.uk*

Abstract: A modality of down-conversion leader-follower optical coherence tomography (OCT) is evaluated for delivering an *en-face* OCT image when the photodetected signal pulsates at 4-9 GHz. *En-face* images are demonstrated from an object extending over 1.6 cm employing an I&Q demodulator and a digitizer of only 250 kS/s when using a VCSEL swept source at 100 kHz. The method presented responds to the need to provide guidance in adjusting the position and orientation of the sample to be investigated in front of the scanning head of a fast swept-source OCT system that, due to the combined effect of sweeping speed and large data, cannot provide images in real-time.

Published by Optica Publishing Group under the terms of the Creative Commons Attribution 4.0 License. Further distribution of this work must maintain attribution to the author(s) and the published article's title, journal citation, and DOI.

1. Introduction

The conventional method of swept source optical coherence tomography [1] (SS-OCT) employs a high frequency rate digitizer and a Fourier transform (FT) block [2]. Generally, due to nonlinearity in sweeping and due to dispersion left uncompensated in the OCT interferometer, the spectrum modulation is chirped. A variable rate clock or resampling of data is usually employed to organize data in equal slots along the wavenumber coordinate before the FT.

A different method is that of leader follower (LF) [3] and complex leader follower (CLF) [4], where data are used as acquired, without the need for resampling. Instead, for each depth of interest, a signal processor is used to multiply the photodetected signal with a digitally stored signal, termed as mask. The mask represents the channeled spectrum modulation obtained by using a mirror as an object, placed in such a way as to specify a certain value for the optical path difference (OPD) and, consequently, the channeled spectrum modulation frequency.

In conventional SS-OCT, a FT block processes the digitized electrical signal delivered by the photodetector to obtain an A-scan (a reflectivity profile in depth in the sample imaged) [2]. In LF [3] and CLF [4], each processor determines the value of the same A-scan at a discrete OPD value, using a mask for each OPD point of interest within the A-scan.

There has been tremendous progress in the last 5 years in tuning extremely fast, such that signal processing cannot be completed within the time interval of a sweep, preventing real-time display of processed data. In addition, when employing a conventional OCT system [1,2] based on a FT processor, to produce an *en-face* OCT image, all A-scans for all lateral pixels must be acquired first, followed by assembling the A-scans into a volume of the object. Only then, an *en-face* OCT slice can be generated after sectioning the volume at the required depth.

#603788 https://doi.org/10.1364/OE.603788
Journal © 2026 Received 27 Apr 2026; revised 10 Sep 2026; accepted 11 Sep 2026; published 29 Sep 2026

Optics EXPRESS

On the other hand, LF [3] and CLF [4] calculate an *en-face* image for each depth of interest, with no need to assemble the volume of data. This represents an advantage in comparison to the conventional FT-based signal processing. For photodetected signals with frequencies less than 1.5 GHz, both FT based [5–10] and CLF [11–13] methods have progressed using several GS/s sampling rates. For instance, digitizer boards, that can be inserted into PC slots, with up to 8 GS/s exist but their analog input bandwidth barely achieves 1.5 GHz. Due to the combined effect of ultrafast sweeping rates and long coherence length of recently developed swept sources, the frequency of the photodetected signal may exceed 100 GHz, close to the maximum frequency of commercial photodetectors. To handle such high frequency signals, digitizers with similar input bandwidth and high sampling rate are required, which are provided by high-speed digital storage oscilloscopes [14–22]. Wang et al. [20] achieved a 1.5 m imaging range with a 100 kHz axial scan rate and 15 µm depth resolution that required digitizing the interferometric signal directly at 50 GSa/s with a 16 GHz detection bandwidth, as another example of SS-OCT delivering a GHz photodetected signal, but with display only possible post acquisition. In the majority of such reports [14–20], again FT was applied as signal processing with recent CLF applications [21,22]. High sampling rate carries the disadvantage of lower dynamic range, of 8-10 bits instead of the ubiquitous 12 bits employed so far in OCT signal processing, since most digitizers over 8 GS/s have fewer than 12 bits. So even before reaching the extreme value of 100 GHz, for much lower frequencies, when the photodetected signal pulsates at a higher rate than a few GHz, digital signal processing becomes a problem. Therefore, for real-time display, Down-conversion Leader Follower (DLF) method was introduced [23–25]. This implements the Leader Follower (LF) protocol where the mask is produced by using an interferometer, termed as leader, driven by the same swept source as the OCT interferometer. An analog multiplier is employed to produce multiplication of the OCT signal with that of the mask. The analog multiplier [23] together with the leader interferometer (LI) and a photodetector constitutes a processor for the OPD value of the LI. A DLF system with three interferometers based on two LIs and a follower interferometer (FI), producing two real-time *en-face* views from two specified OPD values was also reported [24]. The output signal from the analog multipliers pulsates at the frequency difference of the two signals present in the FI and LI. This is within a bandwidth comparable with the sweeping frequency, i.e. much lower than the bandwidth of the OCT signal. Therefore, the DLF procedure reduces the demand for a high-speed digitizer. In addition, the chirp due to the nonlinearity in tuning, $g(k)$, is incorporated into the masks experimentally produced by the LIs. Extra processing, such as resampling or using a clock [5–10] when employing the conventional FT based processing are not needed.

In [25], the sweeping rate (1/T) was only 100 kHz, but with a coherence length exceeding 10 cm, a multi-GHz signal was produced. By the time of the experiment the lack of a high-speed digitizer was compensated by performing DLF. However, the previous reports on DLF [23,24] referred mainly to the simplification in production of *en-face* OCT images using analog multiplication. They did not take advantage of the frequency downconversion, as the signal frequency did not exceed 1.5 GHz, that was still within the range of 12 bits digitizers. Therefore, cross sections could still be produced fast in real time and *en-face* views at the rate of volume acquisition, in a few seconds. Here, for the first time, we illustrate the DLF processing photodetected signals of much higher bandwidth, approaching 9 GHz, where OCT cross sections could not be produced in real time. Such a high frequency would have required a digitizer sampling at over 18 GS/s and an input front end with an analog bandwidth of over 9 GHz. 12-bit digitizers with such parameters do not exist. Previously reported papers on SS-OCT using sweeping lasers faster than a few MHz used digital storage oscilloscopes [15–19,21,22]. They may sample fast and they may have the necessary analog input bandwidth, but the data generated by sampling is so large, that production of A-scans cannot be done in a sweep time interval T, hence their image delivery is not in real time. Even more, the data needs to be transferred from the acquisition card to the computer to be

Optics EXPRESS

processed. With digital storage oscilloscopes, the data is stored locally, extending the time of processing of A-scans, B-scans and volumes to over a minute, i.e. negating the possibility of any real-time display. Therefore, all reports quoted on the right-hand side of Fig. 1 demand an analog bandwidth over 2 GHz and represent OCT systems that are not real time. The references placed on the map in Fig. 1 are based on the information provided in each report in terms of analog bandwidth and sampling rate needed. There is a cluster of references based on digitizers placed inside PCs covering the range of analog signals up to 2 GHz and sampling rate up to 4 GS/s, compatible with real-time display. As for the bit depth range which decreases with the sampling rate, see Fig. S1 in the Supplement 1.

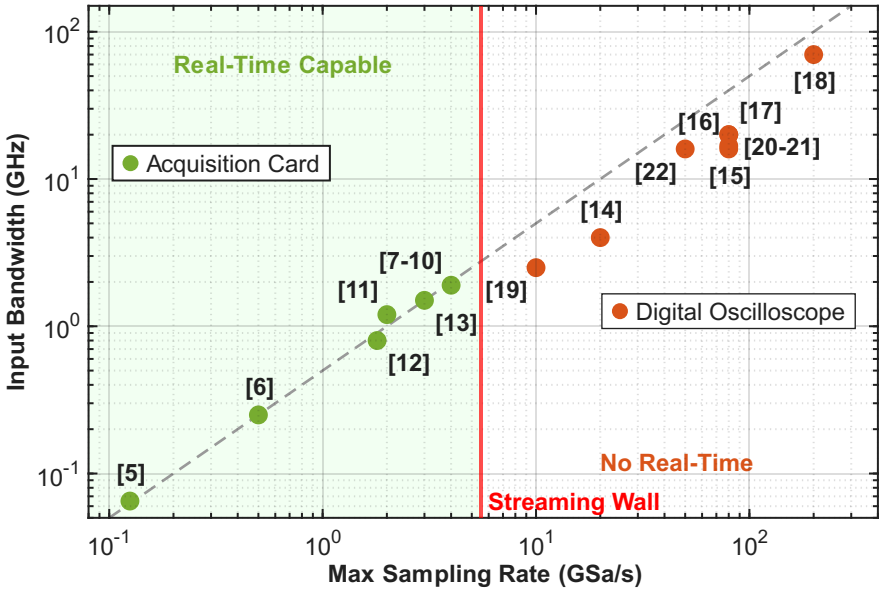


Fig. 1. Scatter plot of prior references on SS-OCT in the plane of analog input bandwidth of the digitizer and maximum sampling rate of the digitizer employed.

The map in Fig. 1 presents a clear division of prior fast acquisition reports into two categories in terms of image display, real time (left) and not real time (right).

This paper reports a DLF SS-OCT system that can be employed to produce *en-face* images in real time even when the frequency of the photodetected signal reaches 9 GHz. In other words, given the high frequencies involved, the system subject of this paper would belong to the right-hand side of the plot in Fig. 1 [14–22], but provides *en-face* OCT images in real-time. Real time provision of A-scans and B-scans was a capability for the reports of much slower speed only, mapped on the left-hand side of Fig. 1.

As shown further below (section 3.4), a DLF configuration presented can be used in parallel to any flying spot SS-OCT system, including those on the left as well as on the right of Fig. 1. However, most useful for the DLF is to be added to an SS-OCT system using a high sampling rate digital oscilloscope [15–22] (right-hand side of Fig. 1) to provide real-time display of an *en-face* OCT image. To prove the affordability of the hardware combination, *en-face* real time imaging of an axially extended object is demonstrated here. The sampling rate needed for signal delivered by the analog multiplier at the core of the DLF channel is in the range of the tuning speed of the swept source only (i.e. 100 kHz), while the photodetected signal contains frequencies from 100 kHz to 9 GHz. Such a system, on its own or as an add-on would be useful to deliver at least an *en-face* slice in real time when the sweeping rate is large, exceeding tens of MHz. If the

Optics EXPRESS

tuning laser employed exceeds several tens of centimeters coherence length, even when sweeping at sub-MHz rates, but imaging at large OPD values, the frequency of the photodetected signal could easily exceed 2 GHz in which case such a DLF system on its own or as an add-on could deliver at least an *en-face* slice in real time. Such a case is presented here, for a high coherence VCSEL swept source at 100 kHz employed to acquire data for large OPD values leading to frequencies exceeding 9 GHz. The authors are not aware of any other established depth resolved OCT approaches that can work in real time at such a high frequency.

2. Experimental set-up

The system employed for this study is schematically presented in Fig. 2. In Fig. 2(a), the block diagram of a DLF-OCT system is shown. A MEMS-VCSEL swept-wavelength laser source (SS, SL13 Series, Thorlabs) 1300 nm central wavelength, tuning at 100 kHz, and coherence length larger than 1 m is employed. The light at the SS output is sent to an optical isolator (Iso) to protect the SS from destructive back reflections and ensuring signal stability. From the isolator, the light is split by a directional coupler (DC), 50/50 towards two interferometers, denominated as a FI and a LI. The balanced photodetected signals from the two interferometers are sent to a multiplier block that performs analog multiplication and, in this way, down-conversion. The multiplier block feeds a digitizer in a PC for image generation. On its inputs, two high pass filters (HPF)s (1400 - 8000 MHz, VHFG-1230 + from Minicircuits) are used to eliminate the bias and the low frequency variations of the photodetected signals from FI and LI, O_F and O_L respectively. Output of both HPFs in FI and LI are sent to a wideband, high linearity I/Q demodulator acting as an active multiplier (X, Analog Devices, LTC5594, 300 MHz to 9 GHz frequency range). The outputs of the multiplier X (I_+, I_-, Q_+ and Q_-) are sent to differential amplifiers DAI and DAQ to produce $I = I_+ - I_-$ and $Q = Q_+ - Q_-$ signals respectively [23,24]. Their outputs are sent to low pass filters, *LPFI* and *LPFQ* (Stanford Research, LNA SR560), producing $<I>$ and $<Q>$.

The Q signal is the result of the multiplication of the two input signals from FI and LI, while the I signal is the result of the multiplication of the same input signals, with one of them out of phase by 90^0. Full characterization of the multiplier is presented in Figs. S2, S3, S4 and S5 in the Supplement 1. The output signals of the *LPFI* and *LPFQ* ($< I >$ and $<Q >$) are sent to a data acquisition board (National Instruments PCIe-6321), sample rate of 250 kS/s, which, when coupled with a custom-made acquisition LabVIEW software, yields 500×500-pixel *en-face* images at a rate of 1 s per frame. The *en-face* rate is the same as that of the volume rate of data otherwise acquired with the SS-OCT system employing the digital scope. Real time processing here means that brightness is calculated for each lateral pixel in the *en-face* OCT image in the sweep period T = 1/100 kHz = 10 µs.

The internal structure of the two interferometers is shown in Fig. 2(b). In the object arm of the FI, a dual galvanometer scanning head (Han's Scanner ST series, Shenzhen Han's Scanner S&T Co., Ltd.) is used to scan the optical beam over the sample, via a lens L which has a 75 mm focal length (Thorlabs Achromatic Doublets AC508-075-C). In each interferometer (FI and LI), light is split into a sample arm and into a reference arm using a 20/80 DC1. Optical power from the SS is 25 mW, after the isolator is ~ 22 mW and power output of the sample arm in the FI is 1.9 mW. In both interferometers, inline fiber polarization controllers (PolC) are installed. The two waves from the reference and sample arms in the two interferometers are combined in a 50/50 DC2. Light from fiber is collimated to free space by New Focus aspheric lenses C (15 mm focal length) apart from that focusing lens after the scanning head in the FI. The outputs of FI and LI feed identical balanced photodetectors BPF and respectively BPL (Optilab, Model BPR-22-M, DC to 22 GHz).

Adjustment of OPD in each interferometer is performed via translation stages TSF and TSL in the respective FI and LI. Due to the configuration of the launchers, any OPD due to a different depth z in the sample arm corresponds to $2z$ in the reference arm. The *en-face* image

Optics EXPRESS

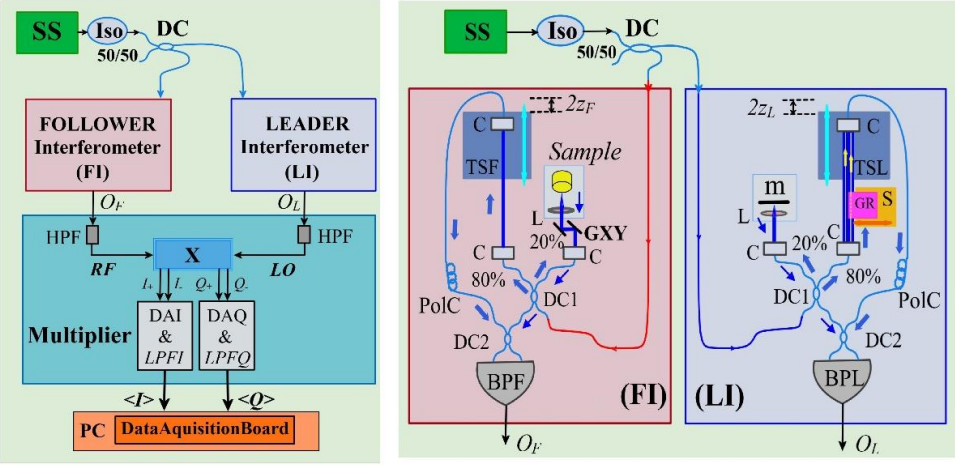


Fig. 2. (a) Schematic diagram of the DLF-OCT system; (b) Detailed structure of the two interferometers. SS: Swept Source; Iso: Optical Isolator; DC, DC1, DC2: directional couplers; FI: follower interferometer; LI: leader interferometer; O_F: photodetected signal generated by FI; O_L: photodetected signal generated by LI; HPF: high pass filter; X: *I&Q* multiplier; RF: radio frequency X signal input; LO: X local oscillator input; DAI: differential amplifier for the *I* signal; DAQ: differential amplifier for the *Q* signal; *LPFI*: low pass filter for the *I* signal; *LPFQ*: low pass filter for the *Q* signal; PC: personal computer; C: collimator; L: lens; GXY: galvanometer scanning head; PolC: inline fiber polarization controller; GR: glass rod; S: stage to insert the glass rod in the reference path of the LI for dual *en-face* imaging as explained in section 3.3; TSF: translation stage in FI; TSL: translation stage in LI; z_F and z_L: movement of translation stage in FI and LI respectively; BPF, BPL: balanced photodetectors in FI and LI respectively.

corresponding to a specific axial position is selected by adjusting the OPD in the LI using TSL, according to the DLF principle [23].

Several LabV based *IQ* programs were written to generate real-time *en-face* OCT images on a PC screen. Two main modalities for averaging the signal from the *I/Q* multiplier are employed here. As previously reported in [23,24], real-time average was produced by the low pass filters in two Stanford Research Amplifiers, *LPFI* and *LPFQ*. Then a computer program is employed to implement [24,26]:

$$S_{LPF} = \left[\langle I\rangle^2 + \langle Q\rangle^2\right]^{1/2} \quad (1)$$

using the averaged values of *I* and *Q* provided by the LPFs. Using this method, the axial resolution depends on the cut off of the LPF, according to Fig. S7 (a) in Supplement 1. For the illustrated images, a LPF bandwidth of 300 kHz was selected determining an axial resolution of the *en-face* slices of ~ 40 µm.

Alternatively, averages can be produced digitally for each sweep interval T on the PC for $< I >$ and $< Q >$ as further detailed in Supplement 1. These are implemented in MATLAB using data stored by the digital oscilloscope, obtaining a different quantity S_n (Eq. S1). Therefore, they are not real time. Such calculations are closer to what a FFT does, where a summation of many photodetected signal samples is calculated over the exact sweeping period. Integration of periodic functions over their period leads to zero. Integration of superior orders pulsating at exact multiples of inverse of the sweeping period are also zero. This does not happen when a LPF is used: lowering the cut off in order to reduce contribution of higher-frequency components

Optics EXPRESS

in fact leads to oscillations outside the strict interval of the sweeping period T. The difference between the two equations (1) and (S1) is simply in the averaging procedure, either using a low pass filter as in our previous DLF reports [23,24], or using numerical calculation in MATLAB. Eq. (S1) provides better axial resolution as illustrated in Fig. S7 (b).

The brightness strength for each lateral pixel displayed in the resulting *en-face* OCT image is associated to the value of S_{LPF} for that specific depth and lateral position. The intensity value of each *en-face* pixel corresponds to the S_{LPF} value for each sweep of the swept source. The LabV/IQ program incorporates controls to deliver *en-face* images in synchronism with the signals driving the scanning head in the FI.

3. Experimental results

3.1. Processing the photodetected signal

A digital storage oscilloscope (Teledyne, model WaveMaster 820Zi-B, 20 GHz, 80 GS/s) is used to measure the photodetected signal delivered by the BPF and BPL in the two interferometers, FI and LI respectively, O_F and O_L. Using sampling rates of 80 GS/s, the input front end of the scope operates up to 20 GHz, similar to the bandwidth of the BPF and BPL employed. As the radio frequency spectrum of the photodetected signal is chirped, there is a spread of frequencies, and such a spread is proportional to increasing OPD values in the interferometer. Therefore, in building the graph of frequency versus OPD in Fig. 3(a), a decision needed to be taken on which frequency value had to be used to represent for each OPD value in the graph. When analyzing the chirped spectra, we observed a peak that seemed to remain at the same relative position within the chirp, and so we decided to use that peak as the frequency reference for each OPD value. Using the TSL in the LI, the OPD was adjusted in several increment steps to achieve over 9 GHz modulation. We stopped at 9 GHz due to the limited bandwidth of the *I&Q* multipliers. The graphs in Fig. 3 represent the dependence between the frequency of the photodetected signal and the OPD/2 = z with a slope s = 9 GHz/454 mm = 19.8 MHz/mm. In what follows, the slope s will be used to associate OPD values to the frequency of the photodetected signal.

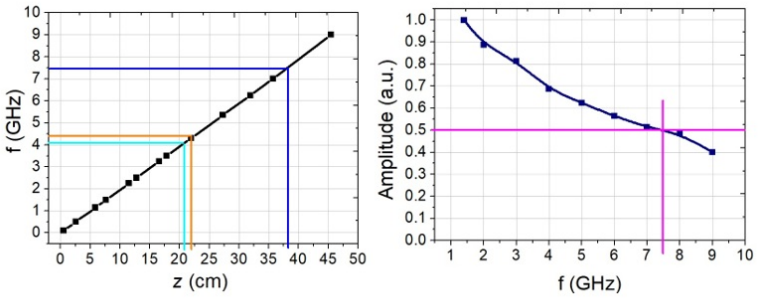


Fig. 3. (a) Variation of the frequency of the FI photodetected signal with z (cm) (either z_F or z_L); (b) Peak to peak amplitude of the FI photodetected signal versus z measured. For the frequency where the graph in (b) reaches half (magenta line) the blue line in (a) leads to a z value of ~ 38 cm; cyan and orange lines in (a) show the range within which the *en-face* OCT images in the Subsection 3.2 were acquired from.

Similar curves are obtained in the LI (not shown). The z coordinate could equally be z_F or z_L. The decay curve in Fig. 3(b) shows that half of the amplitude of the signal is obtained at an OPD/2 = z value of ~ 38 cm, as an approximate measure for the dynamic coherence length of the swept source used. Characterization of the DLF method can be found in Supplement 1 where axial resolution measurements are shown in Fig. S7.

Optics EXPRESS

3.2. En-face OCT images of a 3D printed phantom

In this section, real-time display of *en-face* images from different axial positions is demonstrated, when the frequency of the photodetected signal exceeds 4 GHz. To this goal, a home-made phantom was constructed, utilizing a fused deposition modelling (FDM) 3D printer (QIDI Tech XSmart-3) and polyethylene terephthalate glycol (PETG) filament. The phantom's CAD model lateral and top views are shown in Fig. 4(a) and (b) and its photo in Fig. 4(c). The phantom exhibits three pillars, each engraved with a printed number, *1*, *2*, *3* at the top. The depth of the engravement was set to 250 µm, measured in air. The difference between the heights of the pillars *1* and *2* is ~ 5 mm, similar to the difference in height between pillars *2* and *3*. This value is comparable to or larger than the usual axial range of spectrometer based OCT systems and is within the axial range achievable with commercial MEMS swept sources from Axsun and Santec. The height of pillar *3* measured from the base, being marked with engraved number *4*, is also ~ 5 mm, while the thickness of the base is ~ 1.5 mm. In total, the height of the phantom is 16.5 mm. If the top of pillar *1* had been placed at $z = 0$, all layers could be imaged with conventional SS-OCT systems, as the maximum frequency generated would not exceed 2 GHz. This would correspond to an operation case to the left of the map in Fig. 1, where real-time display would be possible. However, here we use the phantom to illustrate its imaging when $z_F = 20$ cm (mimicking the case of an extended object of over 20 cm), where photodetected signal pulsates at over 4 GHz according to Fig. 3(a). By placing the phantom at a large z value, the operation point is moved to the right of the map in Fig. 1, where using conventional SS-OCT with a digital scope, real-time display cannot be secured. DLF preparation steps for the *en-face* OCT imaging of the 3D printed phantom are presented in Supplement 1 where Fig. S9 shows the frequency selected to perform the experiment, the multiplier outputs and the channeled spectrum in both interferometers LI and FI.



(a) (b) (c) (d)

Fig. 4. Phantom design. (a): lateral view: 16.5 mm total height including the base and 14 mm diameter; 5 mm height difference from one pillar to next; (b): top view of the phantom showing the engraved numbers on top of the pillars; (c): photo of the 3D printed phantom; (d): photo of the lens L in Fig. 1(b) and phantom.

In addition, the signal acquired back into the interferometer fiber from a mirror scanned through focus was measured. This led to a Rayleigh profile width of the interface optics of 2.6 mm (Supplement 1, Fig S6). The axial position of the phantom in relation to the lens L in Fig. 2(b) was adjusted to place the top of pillar *2* in focus. Although the other pillars are outside the Rayleigh range, the focal length of lens L was not changed, as sufficient OCT signal was collected from the other pillars of the phantom, away from the position of best focus. As previously stated, the reference arm in FI was deliberately made larger than the object arm. Therefore, the frequency of the photodetected signal in FI from pillar *1* is larger than the frequency of the photodetected signal coming from pillar *3*. This gives better sensitivity at depth, as larger z values measured along the phantom axis are placed at smaller frequencies. It is known that the sensitivity decays with OPD in SS-OCT; for the system used, this is presented in Fig. S8.

Optics EXPRESS

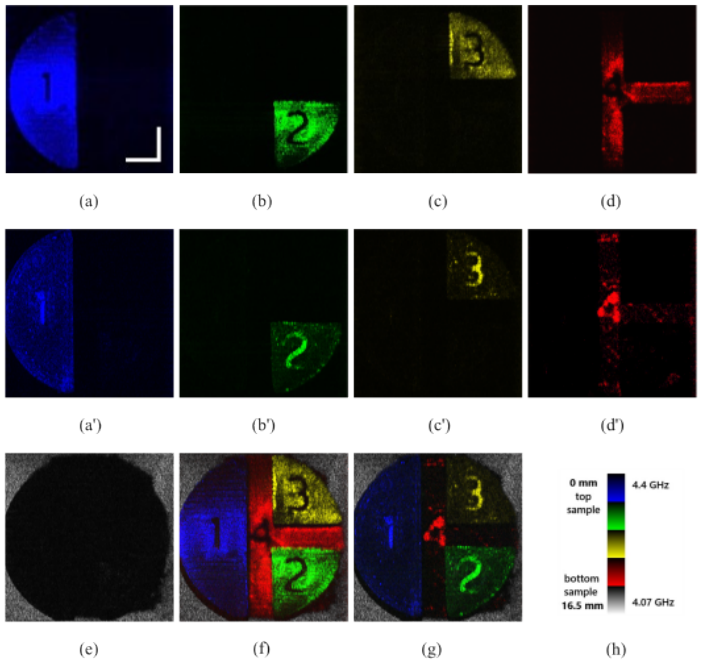


Fig. 5. *En-face* OCT images of the 3D printed phantom obtained using the DLF-OCT system: (a): top of the pillar with engraved print of number *1* displayed, where the frequency of the photodetected signal is 4.4 GHz; (b) top of the second pillar with the engraved print of number *2* displayed, obtained by extending the OPD/2 in the LI by 5 mm in comparison to the value used at (a); (c): top of the 3rd pillar surface with the engraved print of number *3* displayed, obtained by extending the OPD/2 in the LI by 10 mm in comparison to the value used at (a); (d) top of the base with the engraved number *4*, obtained by extending the OPD/2 in the LI by 15 mm in comparison to the value used at (a); (e) *en-face* OCT image of the plate where the sample was laid obtained by extending the OPD/2 in the LI by 1.5 mm in comparison to the value used at (d); (a'), (b'), (c') and (d') *en-face* images obtained by extending the OPD/2 in the LI by ~ 250 µm than respectively in (a), (b), by ~ 380 µm than in (c) and by 260 µm than in (d); (f): superposition of the images in (a), (b), (c), (d) and (e); (g): superposition of the images in (a'), (b'), (c'), (d') and (e'); (h) Color-coded representation of images versus depth from imaging top sample pillar *1* (4.4 GHz), blue navy color, to bottom of the base where the sample sits on (4.07 GHz), gray colored (measured in air), so a total of 16.5 mm was imaged over 327 MHz. Scale bars 3 mm x 3 mm. Lateral image size: 15 mm x 15 mm.

Sequential *en-face* OCT images of the phantom are obtained for different values of the z_L. The images in Fig. 5 are produced when the OPD in LI (OPDL) matches the OPD in the FI (OPDF), i.e. when |OPDL| - |OPDF| = ΔOPD = 0. In Fig. 5(a), (b), (c) and (d), ΔOPD = 0 in each case. Therefore, the engraved numbers are shown as dim in intensity, as the highlighted surface is that of the top of each pillar. In Fig. 5(a'), (b'), (c') and (d'), ΔOPD = 0 corresponds to the bottom of the engraved numbers. Therefore, the engraved numbers are shown in color, surrounded by the darker, lower contrasting PETG substrate. When the OPDL matches the OPDF of the top of the pillar with number *1* feature in the FI, that corresponds to ~ 4.4 GHz modulation of both photodetected signals. When the OPDL matches the OPDF of the top of pillar *3*, the frequency of the photodetected signal is ~ 4.2 GHz. The variation of frequency is in line with the slope of the graph in Fig. 3(a).

Optics EXPRESS

In Fig. 5(e), the *en-face* OCT image of the plate where the sample was laid is displayed while in Fig. 5(f) and (g) the superposition of the five *en-face* OCT images presented in (a), (b), (c), (d) and (e) and respectively in (a'), (b'), (c'), d' and (e). The total distance covered from the *en-face* OCT imaging of the top of the sample displayed in Fig. 4(a) up to imaging the plate where the sample was laid, as displayed in Fig. 5(e), was ~ 16.5 mm. Lateral image size: 15 mm x 15 mm.

Figure 5(a') and (b') display *en-face* images obtained at ~ 250 µm deeper than Fig. 5(a) and (b), while Fig. 5(c') and (d') display *en-face* images obtained at ~ 380 µm and ~ 260 µm deeper than the *en-face* images presented in Fig. 5(c) and (d), respectively. Although the depth in the 3D printer was set to 250 µm, due to the 3D printer's limited resolution (~ 100 µm), the engraving depth of numbers *3* and *4* was deeper than 250 µm. Given the depth of grooves in the phantom imaged here exceeding 100 µm, the axial resolution of ~ 40 µm using Eq. (1) was considered sufficient to resolve the heights of the material and to illustrate the depth resolved capability of the DLF method, as presented in Fig. S7(a) of Supplement 1.

A color bar illustrates the main frequency component of the photodetected signal in the LI (h). Blue starts from the OPD corresponding to the top of pillar *1*, at ~ 4.4 GHz. The *en-face* OCT image of the plate where the sample was laid coincides with 16.5 mm and corresponds to a 4.07 GHz frequency (gray).

To illustrate the affordability of the DLF method, the imaging experiment obtained with the active multiplier was repeated with a passive *I&Q* multiplier and the results are presented in Fig. S10 of Supplement 1. Similar quality of images was obtained despite the lack of amplification on the LI signal.

3.3. *Simultaneous display of two en-face OCT images from different heights of the 3D printed phantom*

A simple experiment is performed to demonstrate simultaneous real-time display of two *en-face* OCT images from two different layers of the 3D printed phantom.

To this effect, as detailed in Fig. 6, a mechanism was incorporated in the LI to insert controllably a glass rod GR as shown in Fig. 2(b). First, let us adjust z_L in the LI to match the OPD in the FI for top of pillar *2* (OPD_A in Fig. 6(a)). Using the active multiplier, an *en-face* OCT image with the engraved print of number *2* displayed was obtained and presented in Fig. 7(a). The next pillar considered was the engraved print of number *3* pillar, which is 5 mm shorter than pillar *2*, so it requires a larger OPD in LI. In order to image pillar *3*, the cylindrical glass rod, GR, shown in Fig. 2(b), is inserted into the reference arm of LI, by actuating on the translation stage S that carries the glass rod. When the GR intercepts the entirety of the reference beam profile (OPD_G in Fig. 6(b)), the *en-face* OCT image presented in Fig. 7(b) is obtained. The cylindrical rod is oriented in such a way that its axis is parallel to the direction of the reference beam. The two circular bases of the rod are in this way perpendicular to the reference beam. To obtain the *en-face* view of the pillar *3*, the length, *t*, of the glass rod was chosen to satisfy the equation:

$$OPD_G - OPD_A = (n-1) \times t = 10 \text{ mm} \quad (2)$$

where n ~1.5168 is the index of refraction of the BK7 glass rod [27]. This leads to t ~ 19 mm. By inserting the glass rod halfway into the beam, the reference beam is divided into two parts, one part through air (OPD_A) and the other through glass (OPD_G), as illustrated in the sketch in Fig. 6(c). In this configuration, with GR halfway inserted into the beam profile, *en-face* OCT images are simultaneously obtained from two heights of the sample. The simultaneous display of two images is achieved using either the active multiplier in Fig. 7(c), or the passive multiplier in Fig. S11 of Supplement 1. So, instead of employing two independent LIs to display simultaneously *en-face* images from two different axial positions, partially inserting a delay in either arm of the LI determines a mask made from the patterns of two channeled spectra corresponding to two OPD values. This procedure can only be applied to single-layer targets.

Optics EXPRESS

The phantom can be considered here as made from an opaque material, in which case in cross section, a single layer is displayed, as penetration along experimental A-scans was minimal. The method produces overlapped images if applied to multilayer targets, such as tissue. An A-scan in the material of the phantom used has shown a penetration less than 1 mm.

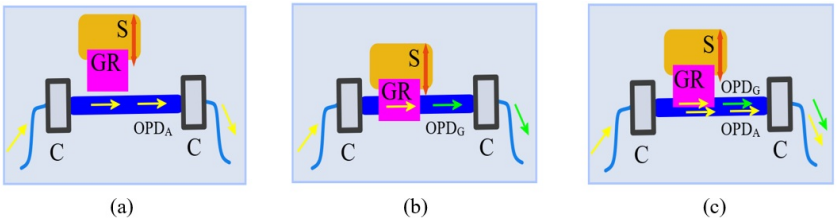


Fig. 6. Sketch of the LI reference arm where a GR of thickness matching the height difference between the second and third pillar is inserted: (a) No Glass: All reference wave rays travel through air only (OPD$_A$); (b) Glass In: All reference wave rays travel through glass only (OPD$_G$); (c) Glass halfway inserted: In its transversal section, the reference beam is divided into two parts, one part through air (OPD$_A$) and the other through glass (OPD$_G$)

The two-depth glass-rod result illustrates a low-cost approach to image different heights of a single-layer object within the transversal section. In Fig. 7 demonstration was performed for an OPD difference matching the exact distance between two relevant heights for the phantom structure investigated here.

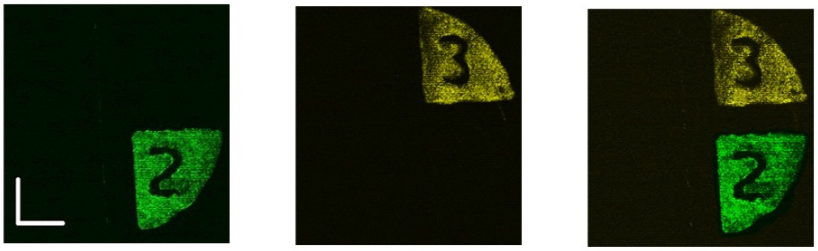


Fig. 7. *En-face* DLF-OCT images of the 3D printed sample obtained using the three positions of the GR glass rod in the reference arm of the LI, as shown in Fig. 6 and using the active multiplier. (a) *en-face* image obtained when the OPD in the LI is adjusted that matches the OPD in air in the FI for pillar *2* (glass rod not inserted, Fig. 6(a)); (b) *en-face* OCT image obtained when the glass rod was inserted into the reference arm of LI, Fig. 6(b); (c) simultaneous display of *en-face* OCT images from the top of pillars *2* and *3* obtained when the glass rod is halfway inserted into the reference arm of LI, Fig. 6(c). Scale bars 3 mm x 3 mm. Lateral image size: 15 mm x 15 mm.

In case guidance is sought in adjusting the position of the object, the procedure can be extended by using several delay elements with thickness calculated using Eq. (2) within a single LI, at the cost of a quantifiable reduction in the reference power for each delay element. Having a few delays created within the LI may ease the initial axial position adjustment of the object. Similarly, for the process of offering guidance in adjustment of the object tilt, having two *en-face* views at the same time from two different OPD values may help in adjusting the orientation of the object facet. For such an application, a single delay, slightly larger than an axial resolution interval may be introduced. Due to tilt, different parts of the object may appear in two patches separated by a gap in the *en-face* slice, due to two coherence gated axial intervals selected from a tilted surface.

Optics EXPRESS

If the facet is oriented perpendicular to the axis, all pixels will become bright at once in one of the two patches. Otherwise, if the sample is multilayer, such as tissue, for correct imaging, several independent LIs should be used. In addition, the dispersion introduced by increased layers of glass deteriorates the axial resolution and reduces the interference strength of the respective created interferometer, but this was not noticeable for the glass rod experiment.

3.4. DLF Add-on block to a fast SS-OCT system

Here, based on the DLF procedure explained above, we refer to an add-on block to a fast or ultra-fast SS-OCT system, to provide guidance in adjusting the object to be imaged by the scanners of the SS-OCT system. Such a solution would be applicable to any fast or ultrafast SS-OCT system on the right-hand side of the map in Fig. 1 [15–22], as shown in Fig. 8, irrespective of its destination, medical imaging or non-destructive testing. The method presented requires tapping some optical power from the swept source and tapping some electrical signal from the photodetector unit of the SS-OCT system in order to provide a guiding depth resolved *en-face* OCT image to the main SS-OCT that performs high resolution volume data acquisition. The add-on can be added to any SS-OCT system reported using FFT [14–19] or using CLF [21], which could not deliver an image in real time (corresponding to the reports located in the right-hand region of the graph in Fig. 1). The role of the fast or ultra-fast SS-OCT system is played by the FI shown in Fig. 8. In the SS-OCT system, the time needed to process B-scans and volumes can take many minutes. For this reason, in [21], where channeled spectra pulsated at over 5 GHz and a 80GS/s digital oscilloscope was used, a time domain (TD) *en-face* OCT procedure was employed to guide the most suitable position and orientation of the sample in front of the scanning head [22]. Switching from SS-OCT to TD-OCT required multiple steps and time.

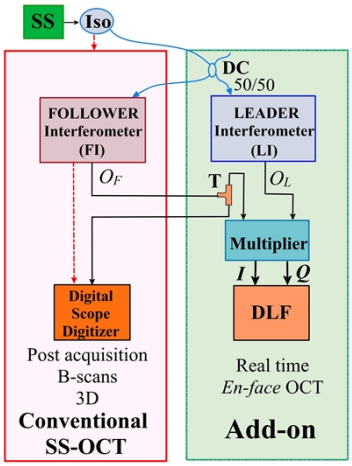


Fig. 8. Schematic diagram of a conventional SS-OCT system employing an ultra-fast digitizer (performed with a digital oscilloscope) to which an add-on block is added to, that performs DLF-OCT for real-time *en-face* OCT imaging. O_F: photodetected signal generated by FI; O_L: photodetected signal generated by LI; T: 18 GHz 50 Ohm matched splitter (Mini-Circuits, model ZFRSC-183-S+)

Therefore, an add-on procedure to a fast flying spot SS-OCT is proposed here, based on DLF, which would be more efficient than the employment of TD-OCT as already reported in [21]. First, as explained below, such an Add-on can work in parallel with the main OCT system, while a tedious sequence of connections was required in [21]. Second, such a system would be superior in sensitivity to TD-OCT, as LF, CLF and DLF-OCT methods belong to the category of spectral

Optics EXPRESS

OCT methods. As shown in Fig. 8, a DLF add-on block is attached to the main SS-OCT system. This requires an optical splitter, DC, to divert light to a second interferometer, LI (similar to that used in Fig. 2) and an electrical splitter, T, to divert some of the photodetected signal from FI, O_F, to a multiplier block similar to that in Fig. 2. While the main SS-OCT based on the FI cannot deliver any information in real time, the DLF Add-on can perform *en-face* OCT at the frame rate of the lateral scanner in the FI. The penalty is a slight reduction of optical power sent to the OCT system (to the FI) and a slight reduction in the amplitude of the electrical signal processed by both systems, the DLF and the conventional SS-OCT system.

As a proof of concept, three A-scans were recorded with the CLF method using the SS-OCT block (left of diagram in Fig. 8). A-scans were obtained with zero voltage applied to both inputs of the scanning head, i.e. with the stationary beam oriented along the optical axis. The phantom was laterally displaced in order to place each pillar in the beam path sequentially and the three A-scans obtained for each case were superposed (Fig. 9). Pillar *1* in yellow was obtained with twice the gain applied to compensate for the loss due to the narrow focus of the lens.

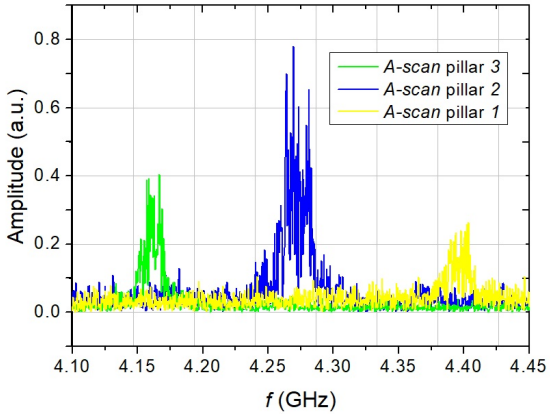


Fig. 9. A-scans obtained from pillar *1* (yellow), *2* (blue) and *3* (green) of the 3D printed phantom.

The A-scans in Fig. 9 prove the functionality of the digital scope to obtain depth resolved images and operate in parallel with the Add-on, detailed in the block at the right of diagram in Fig. 8, despite tapping both the optical and the photodetected signals to drive the Add-on. Producing images based on the A-scans in Fig. 9 will correspond to a system at the right of the map in Fig. 1, incapable of delivering an image in real time. We do not show 3D images with the digital scope as that was already demonstrated in the many references placed to the right of the map in Fig. 1 [14–19,21,22]. In addition, the same digital oscilloscope was employed to obtain images based on CLF-OCT using a much faster swept source [22] (40 and 80 MHz sweeping rates). Essential for the subject of this report is that the Add-on can be added to any conventional flying spot SS-OCT system performing FFT based or CLF based signal processing that produces high resolution cross sections and 3D volumes, where the Add-on is harnessed to guide the proper placement and orientation of the sample to be imaged. The guidance is obtained via a depth resolved *en-face* OCT image produced in real time by DLF-OCT.

Simple calculations show that the reduction in the FI signal otherwise connected to the digital storage oscilloscope is not significant. The experiments above used a 50/50 DC coupler. This contributed to a decrease in the signal in the FI by 6 dB. Then the electrical splitter, T, to tap the electrical signal decreases the signal by 6 dB more. The 6–12 dB estimates quantify the loss in fringe signal amplitude introduced by the optical directional coupler and by the electrical T-splitter, not a loss in sensitivity, that when measured, depends on the noise level. A 12 dB

Optics EXPRESS

electronic (RF) amplification of the FI signal after the T-splitter restores the fringe voltage swing to a level compatible with the digitizer's input range. However, care should be taken in choosing the amplifier in terms of its noise. Such an amplification factor is not excessive and such a combined configuration can be made feasible to operate simultaneously in the conventional SS-OCT as well as in the DLF-OCT regime using the FI as the common part.

On the other hand, if *en-face* views are for guidance only, once the sample has been positioned correctly in front of the scanner, sequential use of the two regimes can be implemented, where the two splitters, the DC and T are removed when performing conventional SS-OCT.

Therefore, if no loss of sensitivity in FI occurs when the taps are removed, this means that the sequential use does not imply any change in the original destination of the FI SS-OCT system. For biomedical operation, a small reduction in the signal may affect the diagnosis quality. Hence it is a matter of choice whether imaging using the SS-OCT system is conducted with the taps on or off. For parallel use, the extra amplifier of 12 dB may raise the noise that could affect the quality of diagnosis.

However, a more powerful swept source may compensate for the losses in the fiber splitter DC required for simultaneous operation.

In addition, in comparison with FI, where interference signal is produced between the weak signal from the sample and the reference wave, in the LI interferometer both waves are strong, where in the object arm of the LI a mirror is used. For a 2.2 mW input to the LI, the amplitude of the interference at the balanced photodetector's output of the LI already exceeds 0.25 V (i.e. over the saturation of the LO input, as documented in Supplement 1, Fig. S2 (a) and (b)). This means that using the current 22 mW swept source, the coupler DC can be changed to 10/90 with 10% towards the LI. This shows that there is reserve in signal towards the FI by reducing the tap towards the LI below 50%, meaning that the loss of 6 dB due to the 50/50 coupler can be easily reduced even with the current swept source to less than 1 dB in principle.

If the sensitivity of the main SS-OCT system is reduced due to tapping of optical and electrical signals, the DLF operation can be performed sequentially. After adjusting the position of the sample, under the guidance of the DLF, the DC coupler can be removed and all optical signal is launched into the FI from the SS and the electrical tap, RF splitter T, is also removed and all electrical signal is sent to the digitizer. The switching involves simple optical fiber connections and electrical connections that take short time. The optical source and the main interferometer, FI, are employed in both circumstances, for SS-OCT and for the combined regime with DLF, when the two taps, optical and electrical, are enabled. The reference path of the main interferometer is the same in both circumstances and no change is required in the sample interface optics of the FI consisting of focusing optics and lateral scanner. The switch from the DLF + SS-OCT to SS-OCT alone does not affect the relative position of the sample to be investigated in respect to the interface optics of the SS-OCT system, once this was optimally settled based on guidance from the DLF + SS-OCT.

The signal in the main SS-OCT decreases by 12 dB when switching from no tap to the tapped configuration in Fig. 8 (i.e. when switching from independent SS-OCT to combined regime, DLF + SS-OCT). The signal in the DLF decreases by 6 dB due to the electrical tap needed by the combined system in Fig. 8 in comparison to the level obtained in Fig. 2. These reductions are eliminated when the two systems are employed sequentially.

For guidance in adjusting the object, the decrease in signal may be tolerated in both systems, otherwise, if imaging is essential, the two taps are removed and the SS-OCT system is used on its own. Also, if imaging is needed by the DLF alone, then the tap to the digitizer is removed and the same sensitivity as that reported above for the system in Fig. 2 is obtained. In either case, the object is considered placed in the optimal way in respect of position and orientation, as adjusted in the initial steps of calibration, when the DLF was used on its own as in Fig. 2 or in combination with the SS-OCT as in Fig. 8.

Optics EXPRESS

These reductions can be directly applied to evaluate the sensitivities of the two systems in the combined regime in Fig. 8, by 12 dB for the SS-OCT and 6 dB for the DLF. Otherwise, as already presented above, there is reserve in the coupling ratio of the coupler DC already, that together with a more powerful source can completely compensate for the 6 dB current reduction due to the optical tap. As for the 6 dB losses in the electrical tap via the T splitter, two emitter followers [28,29] can be used instead with their inputs connected to the balanced receiver of the FI interferometer and with the two outputs towards the digitizer and the I/Q multiplier. An emitter follower produces a voltage on the output emitter similar to that on its transistor base, and the output impedance is low, capable of driving a 50 Ohm load.

4. Discussion

This paper describes a solution for flying spot SS-OCT systems on the right-hand side of the map in Fig. 1 where the photodetected signal exceeds 2 GHz. There are other modalities to produce *en-face* views. A method compatible with a flying spot SS-OCT is to provide guidance in acquisition by using the overall ac component of the photodetected signal. In synchronism with the galvoscanners, an *en-face* overall image is obtained, which approximately corresponds to a superposition of all *en-face* slices from all depths. This however is not a depth resolved image.

Another possibility would be to engage flying spot TD-OCT. However, this will demand a reference path different from that used by the SS-OCT system. TD-OCT operates around OPD = 0 while SS-OCT operates in an axial range away from OPD = 0 [1].

Full field TD-OCT could also be engaged, but imaging would not have pixel to pixel correspondence, as one system, the SS-OCT, employs the pair of galvoscanners, while the other, the TD-OCT system employs, a 2D camera [1]. In addition, the TD-OCT modality would require changing the optical source and, as a method, is less sensitive than the SS-OCT method.

A conceptually related approach of using an analog mixer was demonstrated by Biedermann *et al.* [30], who generated *en-face* SS-OCT images without a Fourier-transform step by mixing the interferometric fringe signal with a linearly frequency-swept reference signal generated electronically in LabVIEW. There are, however, three fundamental differences between the two approaches. First, in our method both the Leader and Follower signals are interferometric in nature, i.e., both are optical signals acquired from actual interferometers via photodetectors, rather than one signal being electronically synthesized. Second, by doing so, the chirp provided by the LI is similar to that generated by the FI, compensating for tuning non-linearities — a capability not addressed in [30]. Third, our approach downconverts fringe frequencies up to 9 GHz. Electrical synthesis of a chirped mask was reported in [31], i.e. having the LI replaced by a relatively low cost electrical synthesizer covering frequencies up to 500 MHz. Electronic synthesizers capable of reaching 9 GHz exist but are prohibitively expensive, which limits the practicality of this route; the LabVIEW-generated reference used in [30] operates at comparatively low frequencies.

A further point of discussion refers to applications of OCT for long range, where the axial resolution is sacrificed in order to fit the sampling rate of digitizers, as in [30]. In this report, a digitizer of 800 MS/s was employed to produce *en-face* images from objects at 53 m away. By reducing the swept bandwidth, the number of cycles in the channeled spectrum is reduced and in this way, the demand for a high frequency analog bandwidth and a high sampling rate. The DLF presented here can offer a solution for detecting objects at large distances where the axial resolution does not need to be compromised to be detected. Such an example is for a SS-OCT that, despite using a low digitizer to handle a low frequency photodetected signal, due to the large amount of data, post processing is possible only, hence not real time. The DLF method presented here can lead to real-time display of a single or more *en-face* OCT slides using one or more LIs.

In the same category of OCT modalities for long axial range and sacrifice of axial resolution to avoid the use of a digital scope [10,32] presents spectral encoding that leads to a small tuning

Optics EXPRESS

bandwidth per spectral window determining the pixel lateral position. Within a small tuning bandwidth of 0.27 nm, a large OPD of tens of centimeters can produce a few hundred peaks. Again, DLF can be used here to accommodate an even larger number of peaks than allowed by the digitizer and enhance the axial range even further.

It should be noted that in applying DLF to produce real-time OCT *en-face* images from a large distance, there is no need to compromise the axial resolution.

5. Conclusions

For the first time, DLF-SS-OCT is employed to display *en-face* OCT images in real time in cases where the photodetected signals pulsate at frequencies larger than the front end bandwidth of commercially available digitizers, as well as larger than the bandwidth that can be sampled by commercially available 12 bit digitizers. For such high frequencies, all references on SS-OCT so far are on the right-hand side of the map in Fig. 1. In such cases, digital oscilloscopes are used that sample fast but data are so large that neither FFT nor CLF could be performed within the interval of a single sweep. Also, the transfer of a large amount of such data requires considerable time, leading to delay between acquisition and image generation that can exceed several minutes. The solution described here offers real-time display of an *en-face* OCT image.

En-face OCT images are also demonstrated from different layers of an object extending over 16 mm, placed at a large OPD value, using the DLF method, i.e. by employing a second interferometer, operating as a LI with the interferometer in the OCT system operating as a FI. Here 16 mm can be considered as being a small part of a more extended object over the axial range covering a few tens of cm.

Furthermore, for single layer objects, instead of employing two LIs in order to display simultaneously *en-face* images from two different axial positions, two *en-face* images from two different OPD values are obtained by splitting the beam across its transversal section in a single LI, to implement a mask for DLF corresponding to a superposition of channeled spectra for two different OPD values. In this way, *en-face* images of two layers separated along z by 5 mm are generated in real time using a single interferometer, performing a task otherwise achieved with two LIs.

The DLF-OCT method presented is in principle limited by the bandwidth of the balanced photodetectors in the FI and LI and not by the sampling rate of the digitizer. In principle, DLF can be applied up to the largest reported bandwidth [33] for photodetectors, ~265 GHz. Signal processing is based on analog multiplication performed by *I*&*Q* multipliers, hence sampling rate needed is as low as the sweeping frequency. The photodetected signal used in this study for imaging is between 4.07–4.4 GHz and measurements are performed up to 9 GHz. In such cases, the digitizer should have operated at least at 8.8 GS/s or respectively at 18 GS/s. When exceeding 4-5 GS/s, digitizers suffer from limited dynamic range, as shown by the map in Fig. S1 in Supplement 1 section, being reduced from 12 to 8 bits or even less. Implementing DLF, the sampling rate needed is not 8.8 or 18 GB/s, but only 200 kB/s, i.e. twice the inverse of the sweeping interval (10 μs) frequency of sweeping. According to the graph of frequency generated versus z, number of spectral points needed is $N = 9\,\mathrm{GHz}/f_S$, i.e. $N = 90{,}000$. By using DLF, via Nyquist correction, the sampling needed is reduced by a factor of N/2 compared with the case where the photodetected signal would be digitized at its base frequency.

Axially more extended objects could equally be imaged through the system by replacing the scanning lens with one of a larger focal length. The axial range of the method in the system demonstrated is limited by the bandwidth of the *I*&*Q* multipliers, to 9 GHz. However, this is not a limit in principle: *I*&*Q* multipliers operating at much larger frequency are available. An even wider availability exists for passive RF mixers that could still be used in the method presented. The utilization of *I*&*Q* multipliers, however, gives better stability against phase fluctuations than a passive RF mixer [24]. A passive mixer gives an output proportional to the sine or cosine of

Optics EXPRESS

the phase, while the squares of the outputs of the I&Q mixer, once added as in Eq. (1), eliminate any phase dependence.

Some parallelism can be made between the downconversion procedure at the core of the DLF method presented here and the reports on circular ranging [34–36], that also perform some sort of downconversion. Circular ranging differs from DLF in goals, output and limitations. Circular-ranging delivers depth-resolved cross-sectional or volumetric information over an extended range, using a form of "optical" subsampling. DLF delivers information from a single depth or an *en-face* image for a single OPD value when adding lateral scanning. In the original circular-ranging OCT report [34], signals from different circular-depth orders can be superposed when the scattering extent exceeds the circular range, for example in weakly attenuating or deeply penetrating samples. Conventional circular ranging also provides relative, rather than absolute, depth; later developments addressed this absolute-depth/order ambiguity [35,36]. It should be said that the DLF method presented here does not suffer from such a problem if multiple independent LIs are used, each generating a single independent mask different from the others. We exclude here the case of the simple experiment with a delay in the LI generating a mask as an equivalent superposition of two masks from two dependent LIs. If tissue were the sample, then the DLF method with delay in the LI would generate overlapped *en-face* images. To avoid the overlap, when imaging multilayer structures, such as tissue, DLF should only be implemented with independent LIs.

We restricted the study to a large object aiming to demonstrate DLF functionality at high, many GHz frequencies. In addition, we limited the main objective to guidance of high resolution, detailed investigation performed by the FI. If *en-face* imaging is targeted of tissue placed at such large distances, we expect to have sensitivity to produce good images as the coherence length of VCSEL secures a high strength of the interference signal from distant objects. However, to acquire signal from a scattering sample would require a better focus, i.e. a larger NA of the interface optics. Deliberately, for the phantom evaluated here, we reduced the NA in the spirit of applications in [10,20,32,33] targeting large objects and large distances, demanding a very small value of the NA of the interface optics (a wide Rayleigh range).

Funding. Medical Research Council (662915, 18557, MR/X502753/1; European Commission (860807); National Institute for Health and Care Research (BRC4-05-RB413-302, NIHR202879); Biotechnology and Biological Sciences Research Council (BB/S016643/1, BB/X003744/1, BB/X511158/1); Engineering and Physical Sciences Research Council (EP/X000125/1).

Acknowledgment. The authors acknowledge support from the DPFS MRC (grant number 662915) awarded to the University of Nottingham and the University of Kent, and from the European Commission through the NETLAS ITN (grant agreement No. 860807). AP also acknowledges funding from the NIHR BRC4-05-RB413-302 at the UCL Institute of Ophthalmology and Moorfields Eye Hospital, as well as support from the NIHR202879 i4i Call 21. Additional funding was provided by the MRC Impact Acceleration Account (project 18557) and MR/X502753/1, the BBSRC grants BB/S016643/1, BB/X003744/1, and BB/X511158/1, including the University of Kent's BBSRC-funded Impact Acceleration Account. Further support came from the EPSRC (FoVEnOCT, EP/X000125/1) and the Imaging, Visual Assessment & Digital Innovation theme at Moorfields Eye Hospital NHS Foundation Trust and the UCL Institute of Ophthalmology. AP generated the idea of the paper. All authors contributed to the acquisition of data, collation and organization of presentation of the study. MM received funding from the Royal Society. AP acted as a PI for the rest of UK grants listed in the funding. AMJ received funding from the Spanish Ministry of Science, Innovation, and Universities. All authors acknowledge Dr. Chao Wang for lending the 40 GHz signal generator.

Disclosures. A. Podoleanu, A. Fernandez and M. Marques are inventors and coinventors of patents in the name of the University of Kent. No other conflict of interest.

Data availability. Data underlying this study are available from the authors upon reasonable request.

Supplemental document. See Supplement 1 for supporting content.

References

1. W. Drexler and J. G. Fujimoto, eds., *Optical Coherence Tomography: Technology and Applications* (Springer, 2008).
2. S. R. Chinn, E. A. Swanson, and J. G. Fujimoto, "Optical coherence tomography using a frequency-tunable optical source," Opt. Lett. **22**(5), 340 (1997).

Optics EXPRESS

3. A. Gh. Podoleanu and A. Bradu, "Master–slave interferometry for parallel spectral domain interferometry sensing and versatile 3D optical coherence tomography," Opt. Express **21**(16), 19324–19338 (2013).
4. S. Rivet, M. Maria, A. Bradu, *et al.*, "Complex master slave interferometry," Opt. Express **24**(3), 2885 (2016).
5. R. Dsouza, H. Subhash, K. Neuhaus, *et al.*, "Dermascope guided multiple reference optical coherence tomography," Biomed. Opt. Express **5**(9), 2870 (2014).
6. T.-H. Tsai, B. Potsaid, Y. K. Tao, *et al.*, "Ultrahigh speed endoscopic optical coherence tomography using micromotor imaging catheter and VCSEL technology," Biomed. Opt. Express **4**(7), 1119 (2013).
7. J. Zhang, T. Nguyen, B. Potsaid, *et al.*, "Multi-MHz MEMS-VCSEL swept-source optical coherence tomography for endoscopic structural and angiographic imaging with miniaturized brushless motor probes," Biomed. Opt. Express **12**(4), 2384 (2021).
8. T. S. Kim, J. Joo, I. Shin, *et al.*, "9.4 MHz A-line rate optical coherence tomography at 1300 nm using a wavelength-swept laser based on stretched-pulse active mode-locking," Sci. Rep. **10**(1), 9328 (2020).
9. S. Chen, B. Potsaid, Y. Li, *et al.*, "High speed, long range, deep penetration swept source OCT for structural and angiographic imaging of the anterior eye," Sci. Rep. **12**(1), 992 (2022).
10. J. Xu, Y. Shi, S. Song, *et al.*, "High-resolution long-range swept-source OCT for volumetric imaging and metrology up to 200 m," Optica **12**(8), 1144 (2025).
11. M. J. Marques, S. Rivet, A. Bradu, *et al.*, "Complex master-slave for long axial range swept-source optical coherence tomography," OSA Continuum **1**(4), 1251 (2018).
12. P. Livens, S. Van der Jeught, J. J. J. Dirckx, *et al.*, "Frequency-dependent assessment of eardrum lesions using multisine OCT vibrometry," Hear. Res. **469**, 109481 (2026).
13. R.-F. Stancu, M. Hughes, T. Sanderson, *et al.*, "Fabrication and testing of lensed fiber-optic probes for distance sensing using common-path low-coherence interferometry," Appl. Opt. **64**(20), 5748 (2025).
14. J.-L. Wu, Y.-Q. Xu, J.-J. Xu, *et al.*, "Ultrafast laser-scanning time-stretch imaging at visible wavelengths," Light:Sci. Appl. **6**(1), e16196 (2016).
15. J. Xu, X. Wei, L. Yu, *et al.*, "High-performance multi-megahertz optical coherence tomography based on amplified optical time-stretch," Biomed. Opt. Express **6**(4), 1340 (2015).
16. A. K. S. Lau, T. T. W. Wong, K. K. Y. Ho, *et al.*, "Interferometric time-stretch microscopy for ultrafast quantitative cellular and tissue imaging at 1 μ m," J. Biomed. Opt. **19**(7), 076001 (2014).
17. J. Kang, P. Feng, X. Wei, *et al.*, "102-nm, 445-MHz inertial-free swept source by mode-locked fiber laser and time stretch technique for optical coherence tomography," Opt. Express **26**(4), 4370 (2018).
18. D. Huang, F. Li, Z. He, *et al.*, "400 MHz ultrafast optical coherence tomography," Opt. Lett. **45**(24), 6675 (2020).
19. I. Akkaya and S. Tozburun, "A 1060 nm stretched-pulse mode-locked wavelength-swept laser source providing an A-scan rate of 20 MHz," Optik (Munich, Ger.) **266**, 169648 (2022).
20. Z. Wang, B. Potsaid, L. Chen, *et al.*, "Cubic meter volume optical coherence tomography," Optica **3**(12), 1496 (2016).
21. A. Martinez Jimenez, S. Grelet, V. Tsatourian, *et al.*, "400 Hz Volume Rate Swept-Source Optical Coherence Tomography at 1060 nm Using a KTN Deflector," IEEE Photonics Technol. Lett. **34**(23), 1277–1280 (2022).
22. A. Martínez Jiménez, S. Grelet, P. Bowen Montague, *et al.*, "Dual ultrahigh speed swept-source and time domain optical coherence tomography system using a time stretch laser and a KTN deflector," in *Optical Coherence Imaging Techniques and Imaging in Scattering Media V*, M. Wojtkowski, Y. Yasuno, and B. J. Vakoc, eds. (SPIE, 2023), p. 9.
23. A. Podoleanu, R. Cernat, and A. Bradu, "Down-conversion en-face optical coherence tomography," Biomed. Opt. Express **10**(2), 772 (2019).
24. R. Cernat, A. M. Jimenez, and A. Podoleanu, "Downconversion master slave optical coherence tomography for simultaneous en-face imaging at two depths," Opt. Express **32**(17), 30756 (2024).
25. M. Marques, R. Cernat, J. Ensher, *et al.*, "Akinetic swept-source master–slave-enhanced optical coherence tomography," Photonics **8**(5), 141 (2021).
26. David M. Pozar, *Microwave Engineering*, Fourth Edition (John Wiley & Sons, 2012).
27. " https://refractiveindex.info/?shelf=specs&book=SCHOTT-optical&page=N-BK7".
28. P. Thomas, M. Grozing, and M. Berroth, "Analog Demultiplexer Operating at up to 200 GS/s Using Four Time Interleaved Switched Emitter Followers with a 50% Duty Cycle Clock," in *2021 IEEE BiCMOS and Compound Semiconductor Integrated Circuits and Technology Symposium (BCICTS)* (IEEE, 2021), pp. 1–4.
29. J. Deza, A. Ouslimani, A. Konczykowska, *et al.*, "65 GHz small-signal-bandwidth switched emitter follower in InP heterojunction bipolar transistors," Electron. Lett. **48**(15), 908–910 (2012).
30. B. R. Biedermann, W. Wieser, C. M. Eigenwillig, *et al.*, "Real time en face Fourier-domain optical coherence tomography with direct hardware frequency demodulation," Opt. Lett. **33**(21), 2556 (2008).
31. A. M. Jimenez, R. Cernat, and A. Podoleanu, "Electrical versus optical generation of leader signals for downconversion leader-follower optical coherence tomography," IEEE Photonics J. **18**(1), 1–14 (2026).
32. R. Qian, K. C. Zhou, J. Zhang, *et al.*, "Video-rate high-precision time-frequency multiplexed 3D coherent ranging," Nat. Commun. **13**(1), 1476 (2022).
33. S. Lischke, A. Peczek, J. S. Morgan, *et al.*, "Ultra-fast germanium photodiode with 3-dB bandwidth of 265 GHz," Nat. Photonics **15**(12), 925–931 (2021).
34. M. Siddiqui, A. S. Nam, S. Tozburun, *et al.*, "High-speed optical coherence tomography by circular interferometric ranging," Nat. Photonics **12**(2), 111–116 (2018).

Optics EXPRESS

35. N. Lippok and B. J. Vakoc, "Resolving absolute depth in circular-ranging optical coherence tomography by using a degenerate frequency comb," Opt. Lett. **45**(2), 371 (2020).
36. S.-K. Chun, H. Jang, S.-W. Cho, *et al.*, "Unfolding displacement measurement method for the aliasing interferometer signal of a wavelength-comb-swept laser," Opt. Express **26**(5), 5789 (2018).